Engineering Structures 195 (2019) 579–590

Contents lists available at ScienceDirect

Engineering Structures

journal homepage: www.elsevier.com/locate/engstruct

Shear stress concentrations in tramway rails: Results from beam theory-based cross-sectional 2D Finite Element analyses

Patricia Hasslinger[a], Aleš Kurfürst[a], Thomas Hammer[b], Edgar Fischmeister[b], Christian Hellmich[a], Stefan Scheiner[a,*]

[a] Institute for Mechanics of Materials and Structures, TU Wien – Vienna University of Technology, Vienna, Austria
[b] Wiener Linien GmbH & Co KG, Vienna, Austria

ARTICLE INFO

Keywords:
Grooved rails
Shear
Torsion
Finite Element method
Damage

ABSTRACT

During their lifetimes, tramway networks become increasingly susceptible to mechanical damage in the form of rail fractures. Understanding the underlying reasons, and initiating appropriate countermeasures may be facilitated by (computational) modeling tools. The development of such tools calls for a sound theoretical foundation. The latter is still largely missing, as the cross-sectional shapes of grooved rails employed in tramway networks differ significantly from those of (in this regard) well-investigated railroad systems. As a first step towards closing this knowledge gap, we here report on a novel beam theory approach allowing to compute typical shear stress distributions throughout the cross sections of grooved rails. Based on classical concepts, such as Bernoulli and Saint-Venant beam kinematics, cross-sectional boundary value problems for the related shear stress distributions are derived, and corresponding solutions are obtained in the form of 2D Finite Element approximations. This way, it is revealed that practically relevant loading scenarios induce distinctive shear stress concentrations. Remarkably, the positions of the latter agree well with fracture patterns observed *in situ*.

1. Introduction

In many urban areas, the tramway network is the backbone of the local public transport system [1–4]. Hence, the reliability of tramway networks is key for the functionality of public life in such areas. The primary causes for disturbances are fractured rails [5,6], as well as degradation due to wear and environmental influences [7,8]. It is evident that rail fractures occur if the loads acting onto the rails induce stress states which exceed the strengths of the steels the rails are made of. A purely experimental approach to the challenge of predicting where and when fractures occur turns out as difficult (if not impossible), given the huge dimensions of the problem (in terms of both size and load magnitude). This calls for computational approaches, and the current state of the art in the field may be briefly sketched as follows: The contact forces between wheel and rail have been quantified for different types of rails (i.e. railroad, subway, and tramway) [5,9–11]. Other modeling approaches are concerned with the estimation of residual stresses. This is often done based on the Finite Element (FE) method, with the main focus lying on Vignole rails [12–18], and an only marginal amount of work spent on tramway rails [19]. Residual stresses have been shown to arise in the rails from the straightening and bending processes prior to mounting the rails [10,12–18,20,21], and change, over time, due to the overrunning by wheels [9–11,22–24], hence under standard operation conditions [22–25]. Numerical methods have also been developed for crack propagation analysis in Vignole rails, either under consideration of residual stresses [27,26], or neglecting the latter [24,28]. The adverse effects of residual stresses may be alleviated by a process called transformation-induced plasticity [17,29], which was also studied numerically [30]. Finally, dynamic effects in train operation have been simulated [35,36], some of which deal with the vibrations caused by tramway operation [37].

In summary, while each of the above-mentioned works deal with phenomena which are of high relevance for the production and operation of rail networks, it turns out that (to the best of our knowledge) the mechanical study of rails in general, and of tramway rails in particular, remains a widely open field, with the available scientific literature being very sparse. The present paper aims at filling this gap. Thereby, the focus is on loading types dominated by shear forces, as they may, for example, arise under abruptly changing embedment conditions. Aiming at an efficient numerical tool for quantifying corresponding shear stress distributions across the cross sections of grooved rails (introduced in Section 2), the following theoretical and

* Corresponding author.
E-mail address: stefan.scheiner@tuwien.ac.at (S. Scheiner).

https://doi.org/10.1016/j.engstruct.2019.03.081
Received 18 April 2018; Received in revised form 26 July 2018; Accepted 25 March 2019
Available online 09 July 2019

computational steps are undertaken: Based on the classical Bernoulli and Saint-Venant beam kinematics, a reduced elastostatics model is derived (in Section 3). The latter gives access to two boundary value problems at the cross-sectional level, one related to shear force-induced shear stresses (see Section 4), and one related to torsion-induced shear stresses (see Section 5). These two boundary value problems are solved for load cases comprising unit shear forces (also included in Sections 4 and 5), as well as for practically relevant load cases, see Section 6. Corresponding results are discussed in Section 7, where also concluding remarks and an outlook to reasonable model extensions and improvements are presented.

2. Definition of studied type of rail

The present study is concerned with the grooved rails used in the Viennese tramway system, in particular with the three profiles shown in Fig. 1, denoted by 60R1, 60R3, and 63R1 [21,31–34]. Notably, profile 60R3 is usually applied in straight tracks, profile 63R1 is usually applied in curved rail tracks, and profile 60R1 is used in straight as well as in curved rail tracks. Standardly, rails used in straight tracks are made of self-hardening steel, whereas rails used in curved tracks are made of heat-treated steels. The heat treatment implies accelerated cooling of the rail heads, which, strictly speaking, results in non-homogeneous, graded distributions of the microstructure across such rails [38–40].

In the current contribution, we focus on the effects of the rail geometry and of the loading on the elastic behavior of rails (on the cross-sectional level). Hence, merely the stiffness of the rail steel is needed as material property entering the subsequently elaborated model. We consider an isotropic and homogeneous stiffness of the rail steel (despite the aforementioned heterogeneous microstructure which is to be expected across heat-treated rails), defined (at room temperature) through a Poisson's ratio of $\nu = 0.28$, and a Young's modulus of $E = 210$ GPa [41,42]. This choice was confirmed for ferritic-pearlitic steels by means of resonant ultrasonic spectroscopy [43], for SS400 and SM490 steels by means of nanoindentation [44,45], and for ferritic iron by means of tensile mechanical tests [46,47]. Notably, the aforementioned elastic constants E and ν correspond to the bulk modulus K via $K = E/[3(1-2\nu)] = 159.09$ GPa, and to the shear modulus G via $G = E/[2(1+\nu)] = 82.03$ GPa.

3. Bernoulli and Saint-Venant beams – reduced elastostatics model

Our theoretical considerations start with the ubiquitiously used beam theories of Bernoulli and Saint-Venant [48], which are, strictly speaking, only valid for constant bending and torsional moments; but which are nevertheless practically relevant for moderately changing bending and torsional moments along the beam axis, i.e. in direction $\mathbf{e}_x$ of an orthonormal base frame $\mathbf{e}_x$, $\mathbf{e}_y$, $\mathbf{e}_z$; with location vectors being denoted as $\mathbf{x} = x\,\mathbf{e}_x + y\,\mathbf{e}_y + z\,\mathbf{e}_z$, see Fig. 2. In more detail, we consider a prismatic beam, and adopt several well-known relations, introduced next:

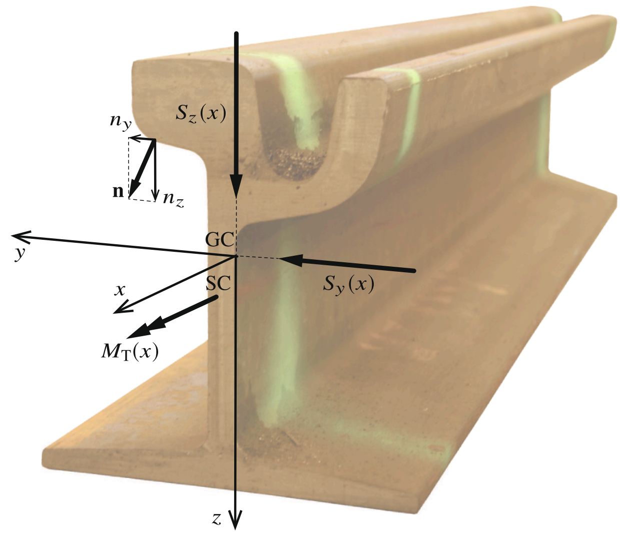

Fig. 2. Photograph of a 60R1 profile (courtesy of Wiener Linien GmbH & Co KG), with indication of stress resultants giving rise to cross-sectional shear stress distributions: horizontal shear force $S_y(x)$, vertical shear force $S_z(x)$, and torsional moment $M_\mathrm{T}(x)$.

- The relation between shear forces $S_y(x)$ and $S_z(x)$, and the corresponding, bending-related normal stress component $\sigma_{xx}(\mathbf{x})$ is given in the format [49–51]

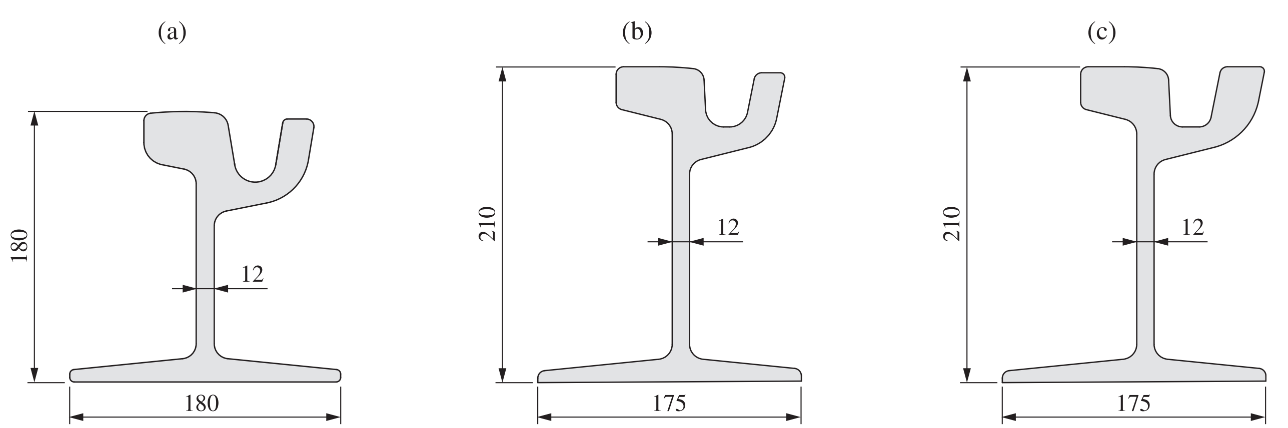

Fig. 1. Grooved rail profiles used in the Viennese tramway network: (a) 60R1, (b) 60R3, and (c) 63R1, see [21,31–34] for further details on the geometries of these profiles; dimensions (rounded to integer numbers) are given in mm.

$$\frac{\partial \sigma_{xx}(\mathbf{x})}{\partial x} = a_y(x)\, y + a_z(x)\, z, \tag{1}$$

with proportionality factors $a_y(x)$ and $a_z(x)$ defined as

$$\begin{bmatrix} a_y(x) \\ a_z(x) \end{bmatrix} = \frac{1}{A_{yy}A_{zz} - A_{yz}^2}\begin{bmatrix} A_{zz} & -A_{yz} \\ -A_{yz} & A_{yy} \end{bmatrix}\begin{bmatrix} S_y(x) \\ S_z(x) \end{bmatrix}, \tag{2}$$

and with the shear forces $S_y(x)$ and $S_z(x)$ being related to shear stress components $\sigma_{xy}(\mathbf{x})$ and $\sigma_{xz}(\mathbf{x})$ via

$$S_y(x) = \int_A \sigma_{xy}(\mathbf{x})\, d\Omega, \tag{3}$$

and

$$S_z(x) = \int_A \sigma_{xz}(\mathbf{x})\, d\Omega. \tag{4}$$

In Eqs. (3) and (4), Ω denotes the cross-sectional domain, whereas A denotes the cross-sectional area. Furthermore, in Eq. (2), A_{yy}, A_{zz}, and A_{yz} are the second-order area moments, defined by

$$A_{yy} = \int_A y^2\, d\Omega, \tag{5}$$

$$A_{zz} = \int_A z^2\, d\Omega, \tag{6}$$

and

$$A_{yz} = \int_A yz\, d\Omega, \tag{7}$$

see Table 1 for the numerical values characterizing the profiles illustrated in Fig. 1. Thereby, coordinates y and z are measured from the geometrical center; i.e. they are related to an arbitrarily translated coordinate system $\bar{y}$, $\bar{z}$ through

$$\bar{y}_{GC} = \frac{1}{A}\int_A \bar{z}\, d\Omega, \tag{8}$$

and

$$\bar{z}_{GC} = \frac{1}{A}\int_A \bar{y}\, d\Omega. \tag{9}$$

- Shape preservation of cross sections during shear and torsional deformation is expressed mathematically via a vanishing shear strain component $\varepsilon_{yz}(\mathbf{x})$,

$$\varepsilon_{yz}(\mathbf{x}) = 0. \tag{10}$$

- The relation between shear forces $S_y(x)$ and $S_z(x)$, acting at distances z_{SC} and y_{SC} from the shear center, and the corresponding (primary) torsional moment M_T reads as

$$M_T(x) = S_z(x) y_{SC} - S_y(x) z_{SC}, \tag{11}$$

with y_{SC} and z_{SC}, the coordinates of the shear center, following from

$$y_{SC} = \frac{G}{S_z}\int_A \left\{\left[\frac{\partial \omega^S(y, z; S_y = 0, S_z)}{\partial z} - \frac{2\nu}{E} a_y(S_y = 0, S_z) y z\right] y - \left[\frac{\partial \omega^S(y, z; S_y = 0, S_z)}{\partial y} - \frac{2\nu}{E} a_z(S_y = 0, S_z) y z\right] z\right\} d\Omega, \tag{12}$$

and

$$z_{SC} = \frac{G}{S_y}\int_A \left\{\left[\frac{\partial \omega^S(y, z; S_y, S_z = 0)}{\partial y} - \frac{2\nu}{E} a_z(S_y, S_z = 0) y z\right] z - \left[\frac{\partial \omega^S(y, z; S_y, S_z = 0)}{\partial z} - \frac{2\nu}{E} a_y(S_y, S_z = 0) y z\right] y\right\} d\Omega. \tag{13}$$

In Eqs. (12) and (13), ω^S denotes the shear warping function; in the general case, this function depends not only on y and z, but also on the coordinate along the beam axis, x. Furthermore, it should be noted that computation of y_{SC} (or z_{SC}, respectively) requires consideration of an arbitrary but non-zero shear force S_z (or S_y, respectively), while S_y (or S_z, respectively) is set to zero.

- Considering primary torsion, a torsional moment $M_T(x)$ induces a constant twist, $\vartheta(x) = \vartheta$, defined through

$$\vartheta = \frac{M_T(x)}{G\, I_T}, \tag{14}$$

with the torsional inertia moment reading as

$$I_T = \int_A \left[(y - y_{SC})\left(y - y_{SC} + \frac{\partial \omega^{M_T}(y, z)}{\partial z}\right) + (z - z_{SC})\left(z - z_{SC} - \frac{\partial \omega^{M_T}(y, z)}{\partial y}\right)\right] d\Omega, \tag{15}$$

see Table 1. In Eq. (15), $\omega^{M_T}(y, z)$ denotes the torsional warping function, defined such that the corresponding shear strain components fulfill

$$\varepsilon_{xy}(\mathbf{x}) = \frac{1}{2}\vartheta\left[\frac{\partial \omega^{M_T}(y, z)}{\partial y} - (z - z_{SC})\right], \tag{16}$$

and

$$\varepsilon_{xz}(\mathbf{x}) = \frac{1}{2}\vartheta\left[\frac{\partial \omega^{M_T}(y, z)}{\partial z} + (y - y_{SC})\right]. \tag{17}$$

Adoption of Eqs. (1)–(17) implies the reduction of the standard governing equations of elastostatics to the following set of 12 equations:

- An adapted set of six compatibility conditions specified for the constraint given in Eq. (10),

$$\frac{\partial^2 \varepsilon_{xx}(\mathbf{x})}{\partial y^2} + \frac{\partial^2 \varepsilon_{yy}(\mathbf{x})}{\partial x^2} - 2\frac{\partial^2 \varepsilon_{xy}(\mathbf{x})}{\partial x\, \partial y} = 0, \tag{18}$$

$$\frac{\partial^2 \varepsilon_{yy}(\mathbf{x})}{\partial z^2} + \frac{\partial^2 \varepsilon_{zz}(\mathbf{x})}{\partial y^2} = 0, \tag{19}$$

$$\frac{\partial^2 \varepsilon_{xx}(\mathbf{x})}{\partial z^2} + \frac{\partial^2 \varepsilon_{zz}(\mathbf{x})}{\partial x^2} - 2\frac{\partial^2 \varepsilon_{xz}(\mathbf{x})}{\partial x\, \partial z} = 0, \tag{20}$$

$$\frac{\partial^2 \varepsilon_{xy}(\mathbf{x})}{\partial x\, \partial z} + \frac{\partial^2 \varepsilon_{xz}(\mathbf{x})}{\partial x\, \partial y} - \frac{\partial^2 \varepsilon_{xx}(\mathbf{x})}{\partial y\, \partial z} = 0, \tag{21}$$

Table 1
Cross-sectional parameters related to profiles 60R1, 60R3, and 63R1, as defined in Fig. 1; the coordinates of the geometrical center, $\bar{y}_{GC}$ and $\bar{z}_{GC}$, are given with reference to the left bottom corner of the cross sections.

Quantity	Unit	60R1	60R3	63R1
A	cm^2	77.15	76.06	80.41
$\bar{y}_{GC}$	mm	97.09	98.98	102.58
$\bar{z}_{GC}$	mm	94.34	112.79	117.13
A_{yy}	cm^4	925.87	839.45	1018.94
A_{zz}	cm^4	3350.88	4744.78	5018.05
A_{yz}	cm^4	237.41	376.99	595.51
y_{SC}	mm	6.03	2.05	7.04
z_{SC}	mm	31.64	32.89	27.27
I_T	cm^4	131.40	110.86	122.58

$$\frac{\partial^2\varepsilon_{xy}(\mathbf{x})}{\partial y\,\partial z} - \frac{\partial^2\varepsilon_{xz}(\mathbf{x})}{\partial y^2} - \frac{\partial^2\varepsilon_{yy}(\mathbf{x})}{\partial x\,\partial z} = 0, \tag{22}$$

and

$$\frac{\partial^2\varepsilon_{xz}(\mathbf{x})}{\partial y\,\partial z} - \frac{\partial^2\varepsilon_{xy}(\mathbf{x})}{\partial z^2} - \frac{\partial^2\varepsilon_{zz}(\mathbf{x})}{\partial x\,\partial y} = 0; \tag{23}$$

- one equilibrium condition in the direction of the beam axis,

$$\frac{\partial\sigma_{xx}(\mathbf{x})}{\partial x} + \frac{\partial\sigma_{xy}(\mathbf{x})}{\partial y} + \frac{\partial\sigma_{xz}(\mathbf{x})}{\partial z} = 0; \tag{24}$$

- three equations related to linearly elastic normal deformations, reading in matrix format as

$$\begin{bmatrix}\varepsilon_{xx}(\mathbf{x})\\ \varepsilon_{yy}(\mathbf{x})\\ \varepsilon_{zz}(\mathbf{x})\end{bmatrix} = \begin{bmatrix}1/E & -\nu/E & -\nu/E\\ -\nu/E & 1/E & -\nu/E\\ -\nu/E & -\nu/E & 1/E\end{bmatrix}\begin{bmatrix}\sigma_{xx}(\mathbf{x})\\ 0\\ 0\end{bmatrix}; \tag{25}$$

- two equations related to linearly elastic shear deformations,

$$\sigma_{xy}(\mathbf{x}) = G\,\gamma_{xy}(\mathbf{x}), \tag{26}$$

and

$$\sigma_{xz}(\mathbf{x}) = G\,\gamma_{xz}(\mathbf{x}), \tag{27}$$

with $\gamma_{xy}(\mathbf{x}) = 2\varepsilon_{xy}(\mathbf{x})$ and $\gamma_{xz}(\mathbf{x}) = 2\varepsilon_{xz}(\mathbf{x})$. From Eqs. (1)–(27), shear stresses arising in response to resultant shear forces acting on tramway rail cross sections can be computed. The corresponding analysis is split into two sub-problems, hereafter referred to as shear and torsional problem, see Sections 4 and 5.

4. Sub-problem I: Shear force-induced shear stresses

We start from expressions for the shear strains $\varepsilon_{xy}(\mathbf{x})$ and $\varepsilon_{xz}(\mathbf{x})$, which, together with Eq. (1), and with the elasticity relations given in Eq. (25), fulfill Eqs. (18)–(23) provided that the shear forces, S_y and S_z, are applied to the beam at a distance x from the cross section under investigation. They read as [51]

$$\varepsilon^S_{xy}(\mathbf{x}) = \frac{1}{2}\frac{\partial\omega^S(\mathbf{x})}{\partial y} - \frac{\nu}{E}a_z(x)yz = \frac{\gamma^S_{xy}(\mathbf{x})}{2}, \tag{28}$$

and

$$\varepsilon^S_{xz}(\mathbf{x}) = \frac{1}{2}\frac{\partial\omega^S(\mathbf{x})}{\partial z} - \frac{\nu}{E}a_y(x)yz = \frac{\gamma^S_{xz}(\mathbf{x})}{2}. \tag{29}$$

Insertion of Eqs. (28) and (29) into the elasticity law for shear stresses given by Eqs. (26) and (27), and of the result, as well as of Eq. (1) into the equilibrium condition given by Eq. (24), while also considering the standard definition of the shear modulus, yields a Laplace-type differential equation of the form

$$G\left[\frac{\partial^2\omega^S(\mathbf{x})}{\partial y^2} + \frac{\partial^2\omega^S(\mathbf{x})}{\partial z^2}\right] = -\frac{a_y(x)y + a_z(x)z}{1+\nu} \quad \text{in} \quad \Omega. \tag{30}$$

Hence, Eq. (30) defines infinitely many boundary value problems in infinitely many y-z planes, with each of these planes being associated to one coordinate value x. For deriving corresponding boundary conditions related to the contour of the cross sections lying in the aforementioned y-z planes, we consider vanishing shear stresses on the contour $\partial\Omega$ of the cross section Ω,

$$\sigma_{xy}(\mathbf{x})n_y\,\mathrm{d}s + \sigma_{xz}(\mathbf{x})n_z\,\mathrm{d}s = 0 \quad \text{on} \quad \partial\Omega, \tag{31}$$

from which the following condition in $\omega^S(\mathbf{x})$ can be derived:

$$G\left[\frac{\partial\omega^S(\mathbf{x})}{\partial y}n_y + \frac{\partial\omega^S(\mathbf{x})}{\partial z}n_z\right] = \frac{\nu}{1+\nu}[a_z(x)n_y + a_y(x)n_z]yz. \tag{32}$$

For solution of the boundary value problem given by Eq. (32), a considerable array of numerical methods is available, both in open scientific literature and in form of commercial software products, including (but not limited to) the Finite Element (FE) method [50,51,52,53], the boundary element (integral equation) method [54,55], and meshless methods [56–59]. In this work, we prefer the FE method due to its computational efficiency, and the straightforward implementability of various boundary conditions, as compared to, for example, meshless methods [60,61].

In particular, for x being fixed, and for given shear forces S_y and S_z, Eqs. (30) and (32) are solved by the FE method. For that purpose, the divergence theorem and integration by parts are applied, yielding the following integral expression:

$$G\int_\Omega \frac{\partial\Phi}{\partial y}\frac{\partial\omega^S(y,z)}{\partial y} + \frac{\partial\Phi}{\partial z}\frac{\partial\omega^S(y,z)}{\partial z}\,\mathrm{d}\Omega$$
$$= \frac{\nu}{1+\nu}\oint_{\partial\Omega}\Phi[a_z n_y + a_y n_z]yz\,\mathrm{d}s + \frac{1}{1+\nu}\int_\Omega \Phi[a_y y + a_z z]\,\mathrm{d}\Omega, \tag{33}$$

with the test function Φ belonging to the test function space $\Upsilon = \{\Phi|\Phi \in \mathscr{H}^1 \text{ in } \Omega,\ \Phi = 0 \text{ on } \partial\Omega\}$, where $\mathscr{H}^1$ denotes the Sobolev space [62]. Since the weak form of sub-problem I, given in Eq. (33), exclusively comprises first-order derivatives, finite elements fulfilling C^0-continuity can be used for discretization of the studied domain. Hence, four-noded quadrilateral finite elements were used, see Fig. 3 for the FE mesh representing profile 60R1 (consisting of 2308 elements). The meshes representing profiles 60R3 and 63R1 consist of 2242 and 2408 finite elements – since they are very similar to the one representing profile 60R1, they are not shown in this paper. The FE discretization was realized by means of the commercial FE software Abaqus (version 6.14), whereas all subsequently described computations were implemented in the commercial mathematics software Matlab (version 2016B), by means of an in-house code.

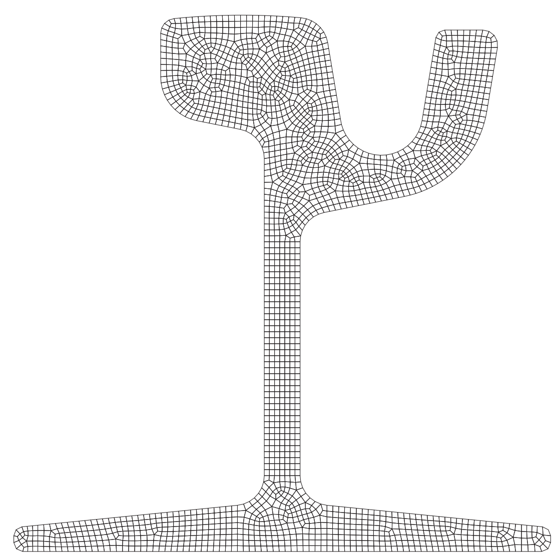

Fig. 3. Exemplary illustration of the FE mesh representing rail profile 60R1, consisting of 2308 quadrilateral finite elements.

Pursuing an isoparametric concept, the element-specific shear warping function $\boldsymbol{\omega}^{S,i}$, the element-specific test function $\boldsymbol{\Phi}^i$, and the element-specific coordinates $\mathbf{y}^i$ and $\mathbf{z}^i$, all of which contain the values relating to the four element nodes, and are hence vectorial quantities, are approximated by the same bilinear shape functions

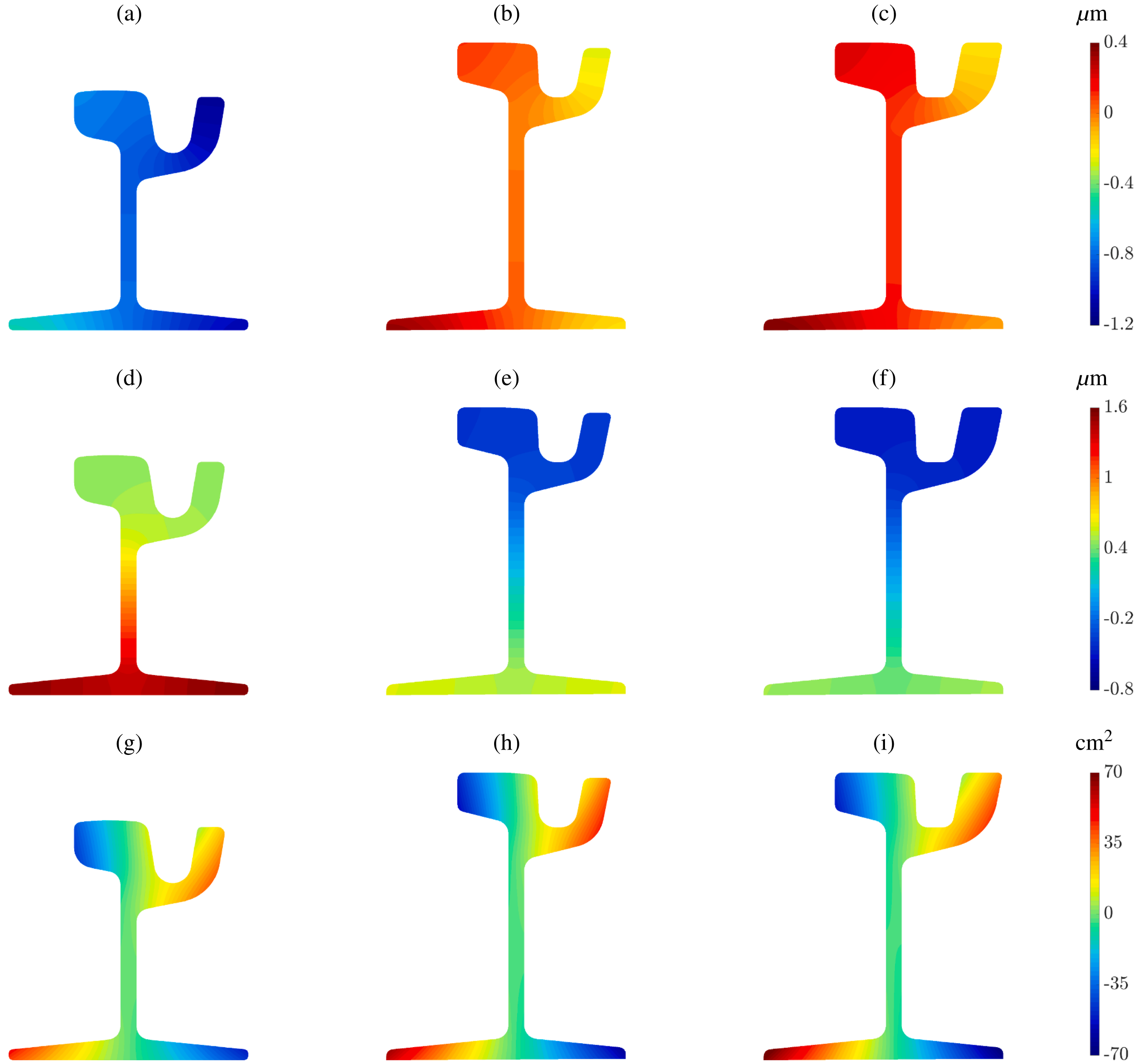

Fig. 4. Computed shear warping functions $\omega^S(y, z;\, S_y = 1\text{ kN},\, S_z = 0)$ for profiles (a) 60R1, (b) 60R3, (c) 63R1, see Fig. 1, and $\omega^S(y, z;\, S_y = 0,\, S_z = 1\text{ kN})$ for profiles (d) 60R1, (e) 60R3, (f) 63R1; (load-independent) torsional warping function $\omega^{M_T}(y, z)$ for profiles (g) 60R1, (h) 60R3, (i) 63R1.

Table 2
Minimum and maximum values of the shear warping functions, $\omega^S(y, z;\, S_y = 1\text{ kN},\, S_z = 0)$ and $\omega^S(y, z;\, S_y = 0,\, S_z = 1\text{ kN})$, and of the torsional warping function $\omega^{M_T}(y, z)$.

Warping functions	Unit	60R1		60R3		63R1	
		min	max	min	max	min	max
$\omega^S(y, z;\, S_y = 1\text{ kN},\, S_z = 0)$	mm	-11.10×10^{-4}	-5.40×10^{-4}	-2.65×10^{-4}	3.41×10^{-4}	-1.95×10^{-4}	3.77×10^{-4}
$\omega^S(y, z;\, S_y = 0,\, S_z = 1\text{ kN})$	mm	6.32×10^{-4}	15.62×10^{-4}	-3.93×10^{-4}	5.95×10^{-4}	-4.97×10^{-4}	4.87×10^{-4}
$\omega^{M_T}(y, z)$	cm^2	−51.94	48.61	−61.80	63.41	−69.59	72.89

$$\mathbf{N} = \mathbf{N}(y, z), \tag{34}$$

interpolating between the element-specific nodal values through [50,63]

$$\omega^{S,i} = \mathbf{N}(y, z)\boldsymbol{\omega}^{S,i}, \tag{35}$$

$$\Phi^i = \mathbf{N}(y, z)\boldsymbol{\Phi}^i, \tag{36}$$

$$y^i = \mathbf{N}(y, z)\mathbf{y}^i, \tag{37}$$

and

$$z^i = \mathbf{N}(y, z)\mathbf{z}^i. \tag{38}$$

Inserting the (approximate) expressions given in Eqs. (35)–(38) into Eq. (33) yields the well-known formulation

$$\mathop{\mathrm{A}}_{i=1}^{n_{\mathrm{el}}} \left[\mathbf{K}^{S,i}\right] \omega^{S} = \mathop{\mathrm{A}}_{i=1}^{n_{\mathrm{el}}} \mathbf{F}^{S,i}, \tag{39}$$

where A denotes the matrix assembly operator and n_{el} denotes the total number of elements. For the shear problem, the element stiffness matrix, $\mathbf{K}^{S,i}$, is defined by

$$\mathbf{K}^{S,i} = G \int_{\Omega^{\mathrm{el}}} \left[\frac{\partial \mathbf{N}}{\partial y}\right]^{T} \frac{\partial \mathbf{N}}{\partial y} + \left[\frac{\partial \mathbf{N}}{\partial z}\right]^{T} \frac{\partial \mathbf{N}}{\partial z} \, \mathrm{d}\Omega^{\mathrm{el}}, \tag{40}$$

and the respective element force vector $\mathbf{F}^{S,i}$ reads as

$$\mathbf{F}^{S,i} = \frac{\nu}{1+\nu} \oint_{\partial\Omega^{\mathrm{el}}} \mathbf{N}^{T} (a_z n_y + a_y n_z)(\mathbf{N} y^i)(\mathbf{N} z^i) \, \mathrm{d}s^{\mathrm{el}} + \frac{1}{1+\nu} \int_{\Omega^{\mathrm{el}}} \mathbf{N}^{T} [a_y (\mathbf{N} y^i) + a_z (\mathbf{N} z^i)] \, \mathrm{d}\Omega^{\mathrm{el}}. \tag{41}$$

The integrals included in Eqs. (40) and (41) were numerically evaluated by means of the Gauss quadrature with 2×2 Gauss points.

The above-described FE model was evaluated in order to compute the profile- and load-specific shear warping functions $\omega^S(y, z; S_y, S_z)$.

(i) for a unit horizontal shear load $S_y = 1\,\mathrm{kN}$ (while $S_z = 0$), see Fig. 4(a)–(c); and
(ii) for a unit vertical shear load $S_z = 1\,\mathrm{kN}$ (while $S_y = 0$), see Fig. 4(d)–(f).

The corresponding minimum and maximum values of the shear warping functions are given in Table 2. Insertion of the shear warping functions computed for case (i) into Eq. (13), and of the shear warping functions computed for case (ii) into Eq. (12) yields the coordinates of the shear center, as given in Table 1.

5. Sub-problem II: Torsion-induced shear stresses

Insertion of torsion-related shear strains following from Eqs. (16) and (17) into the elasticity law given by Eqs. (26) and (27) yields torsion-related shear stresses of the format

$$\sigma_{xy}^{M_{\mathrm{T}}}(\mathbf{x}) = G\,\vartheta \left[\frac{\partial \omega^{M_{\mathrm{T}}}(y,z)}{\partial y} - (z - z_{\mathrm{SC}})\right] \tag{42}$$

and

$$\sigma_{xz}^{M_{\mathrm{T}}}(\mathbf{x}) = G\,\vartheta \left[\frac{\partial \omega^{M_{\mathrm{T}}}(y,z)}{\partial z} + (y - y_{\mathrm{SC}})\right]. \tag{43}$$

Insertion of Eqs. (42) and (43) into the equilibrium condition defined in Eq. (24) yields

$$\Delta \omega^{M_{\mathrm{T}}}(y,z) = 0 \quad \text{in} \quad \Omega. \tag{44}$$

In analogy to sub-problem I, Eq. (44) is complemented by boundary condition

$$\frac{\partial \omega^{M_{\mathrm{T}}}(y,z)}{\partial y} n_y + \frac{\partial \omega^{M_{\mathrm{T}}}(y,z)}{\partial z} n_z = (z - z_{\mathrm{SC}}) n_y - (y - y_{\mathrm{SC}}) n_z \quad \text{on} \quad \partial\Omega, \tag{45}$$

again following from Eq. (31), so that Eq. (44), together with Eq. (45), can be transformed into an integral equation of the form

$$\int_{\Omega} \frac{\partial \omega^{M_{\mathrm{T}}}(y,z)}{\partial y} \frac{\partial \Phi}{\partial y} + \frac{\partial \omega^{M_{\mathrm{T}}}(y,z)}{\partial z} \frac{\partial \Phi}{\partial z} \, \mathrm{d}\Omega = \oint_{\partial\Omega} \Phi [(z - z_{\mathrm{SC}}) n_y - (y - y_{\mathrm{SC}}) n_z] \, \mathrm{d}s, \tag{46}$$

which can be solved by the FE method. Analogously to the FE approach introduced for the calculation of the shear force-induced shear stresses, see Section 4, the weak form of sub-problem II, given in Eq. (46), finally yields the FE-typical formulation

$$\mathop{\mathrm{A}}_{i=1}^{n_{\mathrm{el}}} \left[\mathbf{K}^{M_{\mathrm{T}},i}\right] \omega^{M_{\mathrm{T}}} = \mathop{\mathrm{A}}_{i=1}^{n_{\mathrm{el}}} \mathbf{F}^{M_{\mathrm{T}},i}. \tag{47}$$

For the torsional problem, the element stiffness-like matrix, $\mathbf{K}^{M_{\mathrm{T}},i}$, is defined by expression

$$\mathbf{K}^{M_{\mathrm{T}},i} = \int_{\Omega^{\mathrm{el}}} \left[\frac{\partial \mathbf{N}}{\partial y}\right]^{T} \frac{\partial \mathbf{N}}{\partial y} + \left[\frac{\partial \mathbf{N}}{\partial z}\right]^{T} \frac{\partial \mathbf{N}}{\partial z} \, \mathrm{d}\Omega^{\mathrm{el}} \tag{48}$$

and the respective element force vector $\mathbf{F}^{M_{\mathrm{T}},i}$ reads as

$$\mathbf{F}^{M_{\mathrm{T}},i} = \oint_{\partial\Omega^{\mathrm{el}}} \mathbf{N}^{T} ([n_y (\mathbf{N} \mathbf{z}^i) - n_z (\mathbf{N} \mathbf{y}^i)] \, \mathrm{d}s^{\mathrm{el}}. \tag{49}$$

Again, the integrals given in Eqs. (48) and (49) were numerically evaluated by means of the Gauss quadrature with 2×2 Gauss points.

The above-described FE model was evaluated in order to compute the profile-specific torsional warping functions, see Fig. 4(g)–(i), with the corresponding minimum and maximum values as given in Table 2.

6. Critical loading scenarios: Unit shear forces due to wheel contact

Shear forces with lines of action as seen in Fig. 5 imply torsional moments according to Eq. (11), and resulting shear stresses follow from summation of the shear stresses related to sub-problems I and II, respectively. As regards sub-problem I, the solution $\omega^S(y, z)$, see Fig. 4(a)–(c) and (d)–(f), is first inserted in Eqs. (28) and (29), and the results enter Eqs. (26) and (27), see Fig. 6 for the corresponding shear stresses, and Table 3 for the minimum and maximum values. As regards sub-problem II, the solution $\omega^{M_{\mathrm{T}}}(y, z)$, see Fig. 4(g)–(i), is inserted in Eqs. (42) and (43), see Fig. 7 for the corresponding shear stresses, and Table 4 for the minimum and maximum values.

From the aforementioned unit force-related shear stresses, the effect of any combination of arbitrarily large shear forces can be determined according to the following multi-linear scaling relations:

$$\sigma_{xy} = [\sigma_{xy}^{S}(S_y = S_{y,0}) + \sigma_{xy}^{M_{\mathrm{T}}}(S_y = S_{y,0})] \frac{S_y}{S_{y,0}} + [\sigma_{xy}^{S}(S_z = S_{z,0}) + \sigma_{xy}^{M_{\mathrm{T}}}(S_z = S_{z,0})] \frac{S_z}{S_{z,0}}, \tag{50}$$

and

$$\sigma_{xz} = [\sigma_{xz}^{S}(S_y = S_{y,0}) + \sigma_{xz}^{M_{\mathrm{T}}}(S_y = S_{y,0})] \frac{S_y}{S_{y,0}} + [\sigma_{xz}^{S}(S_z = S_{z,0}) + \sigma_{xz}^{M_{\mathrm{T}}}(S_z = S_{z,0})] \frac{S_z}{S_{z,0}}, \tag{51}$$

where the stress distributions relating to $S_{y,0} = 1\,\mathrm{kN}$ and $S_{z,0} = 1\,\mathrm{kN}$ are shown in Figs. 6 and 7.

It is instructive to perform a corresponding evaluation for a

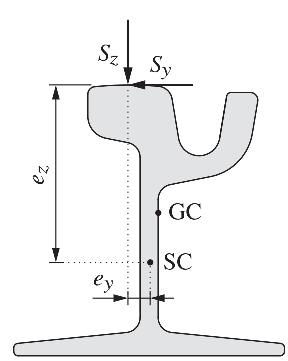

Fig. 5. Loads applied on the rail in curved tracks for computing the primary torsion-related shear stress distributions, shown exemplarily for profile 60R1; abbreviation GC stands for geometrical center, while abbreviation SC stands for shear center.

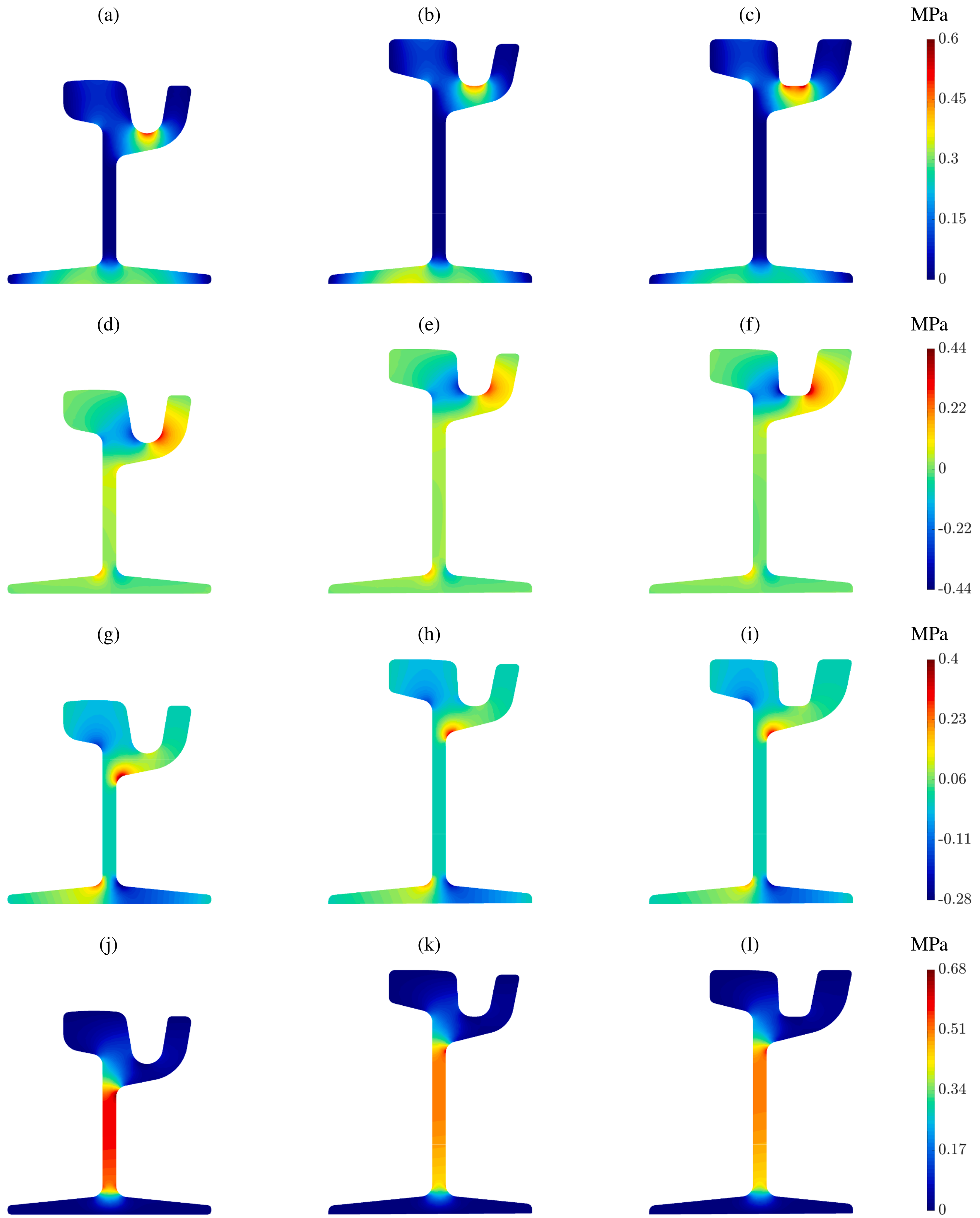

Fig. 6. Computed horizontal and vertical shear force-induced shear stresses: component $\sigma_{xy}^{S}(y, z; S_y = 1\ \text{kN}, S_z = 0)$ for profiles (a) 60R1, (b) 60R3, (c) 63R1; component $\sigma_{xz}^{S}(y, z; S_y = 1\ \text{kN}, S_z = 0)$ for profiles (d) 60R1, (e) 60R3, (f) 63R1; component $\sigma_{xy}^{S}(y, z; S_y = 0, S_z = 1\ \text{kN})$ for profiles (g) 60R1, (h) 60R3, (i) 63R1 and component $\sigma_{xz}^{S}(y, z; S_y = 0; S_z = 1\ \text{kN})$ for profiles (j) 60R1, (k) 60R3, (l) 63R1; compare Fig. 5 for applied loads.

Table 3
Minimum and maximum values (in MPa) of the shear-force induced shear stresses $\sigma_{xy}^S(y, z; S_y = 1\text{ kN}, S_z = 0)$, $\sigma_{xz}^S(y, z; S_y = 1\text{ kN}, S_z = 0)$, $\sigma_{xy}^S(y, z; S_y = 0, S_z = 1\text{ kN})$ and $\sigma_{xz}^S(y, z; S_y = 0, S_z = 1\text{ kN})$ for profiles 60R1, 60R3, 63R1.

Shear force-induced shear stresses	60R1		60R3		63R1	
	min	max	min	max	min	max
$\sigma_{xy}^S(y, z; S_y = 1\text{ kN}, S_z = 0)$	3.45×10^{-4}	5.20×10^{-1}	3.53×10^{-4}	4.70×10^{-1}	2.36×10^{-4}	5.95×10^{-1}
$\sigma_{xz}^S(y, z; S_y = 1\text{ kN}, S_z = 0)$	-2.99×10^{-1}	3.28×10^{-1}	-3.33×10^{-1}	3.03×10^{-1}	-4.11×10^{-1}	4.37×10^{-1}
$\sigma_{xy}^S(y, z; S_y = 0, S_z = 1\text{ kN})$	-2.88×10^{-1}	3.94×10^{-1}	-2.37×10^{-1}	3.27×10^{-1}	-2.35×10^{-1}	3.25×10^{-1}
$\sigma_{xz}^S(y, z; S_y = 0, S_z = 1\text{ kN})$	-8.05×10^{-3}	6.81×10^{-1}	-2.38×10^{-4}	6.07×10^{-1}	-3.17×10^{-4}	6.04×10^{-1}

practically relevant load case, comprising, on the one hand, a vertical load of $S_z = 59.694$ kN, referring to the maximum wheel load of a Viennese tramway car at full capacity [64]. On the other hand, a horizontal load S_y is considered, relating to the centrifugal force that occurs in curved rails sections. For that purpose, we make use of the following relation [65,66]:

$$S_y = \frac{S_z v^2}{R g}, \tag{52}$$

with the gravitational acceleration $g = 9.81\text{ m/s}^2$, the velocity of the wheel v, and the curvature radius R. Here, we consider a velocity of 5 m/s, which is a practically reasonable velocity in curved rail tracks of the Viennese tramway network [67], and the respective minimum rail curvature radius of 18 m [68]. Then, when considering a right-curved track, a horizontal force of $S_y = 16.903$ kN (assuming a movement of the tramway in positive direction of the x-axis, see Fig. 2) can be expected, according to Eq. (52). If the rail embedment abruptly changes from a semi-rigid foundation to a very soft or even missing support, as it may happen in very old tracks or in tracks under maintenance conditions, then the aforementioned forces (S_y and S_z) appear directly as internal shear forces. Hence, it makes sense to insert corresponding values for S_y and S_z in Eqs. (50) and (51); in order to provide access to the respective shear stress distributions. For being able to better interpret the distributions of σ_{xy} and σ_{yz}, the related distributions of von Mises stresses are computed, according to

$$\sigma_{\text{vM}} = \sqrt{3(\sigma_{xy}^2 + \sigma_{xz}^2)}, \tag{53}$$

see Fig. 8 for the profile-specific von Mises stress distributions. The corresponding maximum values amount to $\sigma_{\text{vM}} = 203.06$ MPa for profile 60R1, $\sigma_{\text{vM}} = 230.67$ MPa for profile 60R3, and $\sigma_{\text{vM}} = 189.23$ MPa for profile 63R1. The computed stress concentrations agree well with a failure pattern observed in an 18-year-old rail with profile 60R1 having reached its service life, see Fig. 9; after excavation of the rail, a longitudinal crack appears in the rail web, just below the rail head.

7. Discussion

7.1. Interpretation of results

The 2D FE method presented in this paper gives access to both shear and torsional warping functions. As illustrated in Fig. 4(a)–(c), the shear warping functions due to a unit horizontal shear force $\omega^S(y, z; S_y = 1\text{ kN})$ decrease with increasing y-coordinate, whereas the shear warping functions due to a unit vertical shear force $\omega^S(y, z; S_z = 1\text{ kN})$, see Fig. 4(d)–(f), decrease with increasing z-coordinate. Remarkably, the shear warping functions are not only influenced by the loading but also by the geometry of the cross section. Given that profiles 60R3 and 63R1 differ only in terms of the thicker check rail of the latter, see also Fig. 1(b) and (c), the shear warping functions of these two profiles are also very similar. In turn, profile 60R1 is significantly smaller than the two other profiles studied in this paper, resulting in a substantially different shear warping function distribution. Hence, our results clearly demonstrate the geometry dependence of shear warping functions.

The primary torsional warping functions, in turn, see Fig. 4(g)–(i), are purely geometrical quantities. However, in contrast to the shear warping functions, they do not differ significantly between the studied cross sections. Hence, the torsional behavior of grooved rails turns out to be not so much affected by the exact geometrical dimensions, but rather by their characteristic shapes.

As for the critical loading scenarios presented in Section 6, comparison of the computed von Mises stress distributions to crack patterns observed *in situ* is considered to be a valid approach. For that purpose, we make use of the photograph of a discarded rail section which was thankfully provided by the Wiener Linien GmbH & Co KG. Namely, a rail profile 60R1 is considered, which was excavated from a right-curved rail section after 18 years of operation, see Fig. 9. The computed location of the stress maximum, see Fig. 8(a), agrees well with the location of the crack observed *in situ*, which is in the rail web, just below the rail head.

7.2. Concluding remarks

Building on recent theoretical and computational developments in the relatively old field of beam theories [49–51], the key novelty presented in this paper is the utilization of beam theory for mechanically assessing grooved (tramway) rails – to the best of our knowledge, comparable approaches are not documented in open literature. In particular, shear stress distributions are computed which occur when specific cross sections of such rails are subjected to shear forces, thereby (optionally) also inducing primary (i.e., Saint-Venant-type) torsion.

Moreover, it should be mentioned that the presented approach is extremely versatile. From a conceptual point of view, there is no limitation as to the geometry of the studied cross section; hence, application to other types of rails, or to rails that have undergone some sort of degradation (e.g., due to wear, or corrosion) is quite straightforward.

7.3. Outlook

Considering the modeling concept and the results presented in this paper, several future extensions are desirable, aiming at remedying currently existing limitations:

- The here presented, beam theory-based 2D FE analysis of grooved rail cross sections could be extended into the longitudinal direction, taking thereby into account normal and shear forces, bending moments, and non-uniform (secondary) torsion. Such a fully

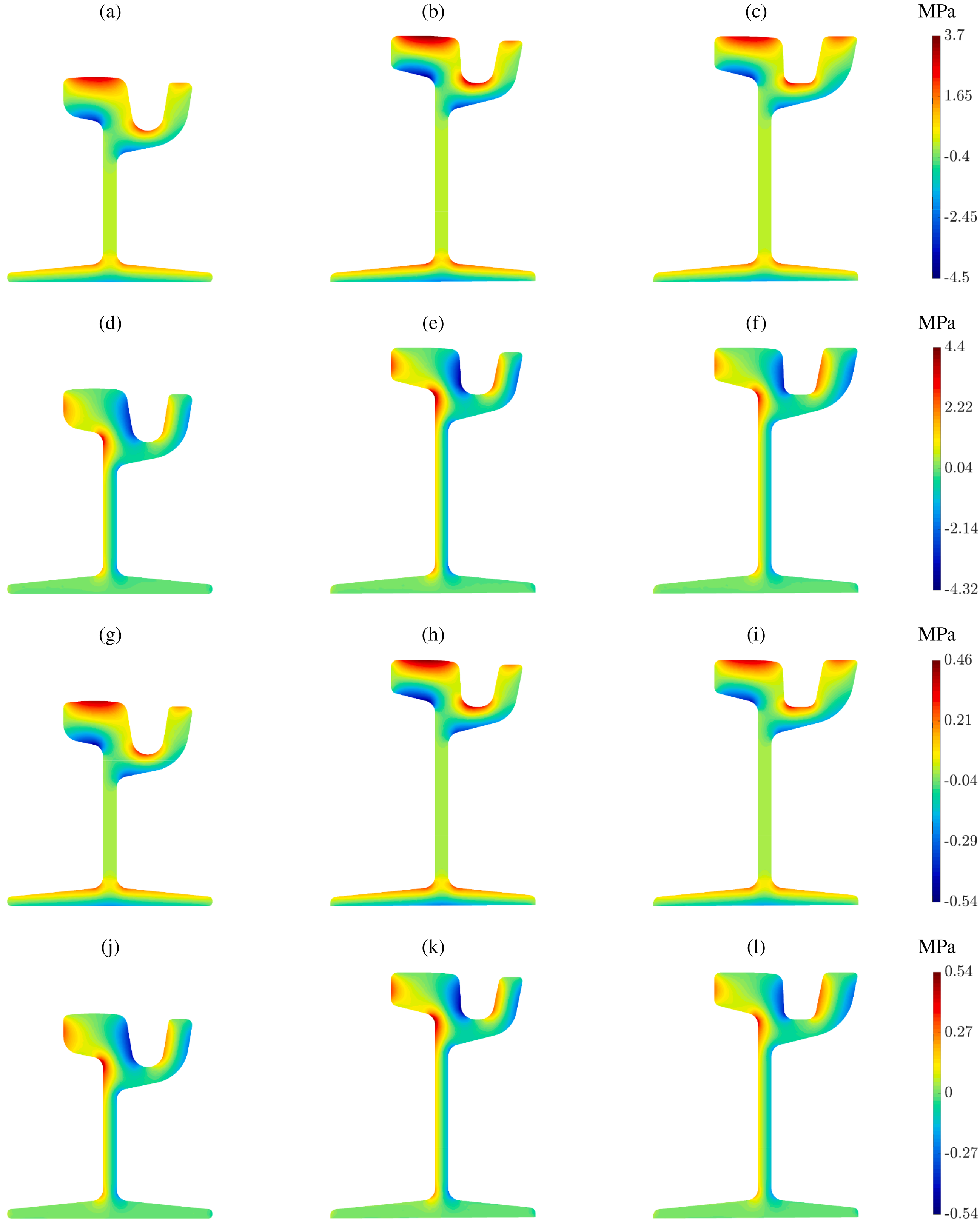

Fig. 7. Computed horizontal and vertical torsion-induced shear stresses due to eccentrically acting shear forces: component $\sigma_{xy}^{M_T}(y, z; S_y = 1\text{ kN}, S_z = 0)$ for profiles (a) 60R1, (b) 60R3, (c) 63R1; component $\sigma_{xz}^{M_T}(y, z; S_y = 1\text{ kN}, S_z = 0)$ for profiles (d) 60R1, (e) 60R3, (f) 63R1; component $\sigma_{xy}^{M_T}(y, z; S_y = 0, S_z = 1\text{ kN})$ for profiles (g) 60R1, (h) 60R3, (i) 63R1; and component $\sigma_{xz}^{M_T}(y, z; S_y = 0, S_z = 1\text{ kN})$ for profiles (j) 60R1, (k) 60R3, (l) 63R1; compare Fig. 5 for applied loads.

Table 4
Minimum and maximum values (in MPa) of the torsion-induced shear stresses $\sigma_{xy}^{M_T}(y, z; S_y = 1\,\text{kN}, S_z = 0)$, $\sigma_{xz}^{M_T}(y, z; S_y = 1\,\text{kN}, S_z = 0)$, $\sigma_{xy}^{M_T}(y, z; S_y = 0, S_z = 1\,\text{kN})$ and $\sigma_{xz}^{M_T}(y, z; S_y = 0, S_z = 1\,\text{kN})$, due to eccentrically acting shear forces for profiles 60R1, 60R3, 63R1.

Torsion-induced shear stresses	60R1		60R3		63R1	
	min	max	min	max	min	max
$\sigma_{xy}^{M_T}(y, z; S_y = 1\,\text{kN}, S_z = 0)$	−3.79	2.91	−4.44	3.64	−3.80	3.03
$\sigma_{xz}^{M_T}(y, z; S_y = 1\,\text{kN}, S_z = 0)$	−3.20	3.58	−4.30	4.39	−3.60	3.63
$\sigma_{xy}^{M_T}(y, z; S_y = 0, S_z = 1\,\text{kN})$	-5.18×10^{-1}	3.97×10^{-1}	-5.40×10^{-1}	4.43×10^{-1}	-4.55×10^{-1}	3.64×10^{-1}
$\sigma_{xz}^{M_T}(y, z; S_y = 0, S_z = 1\,\text{kN})$	-4.38×10^{-1}	4.89×10^{-1}	-5.22×10^{-1}	5.34×10^{-1}	-4.31×10^{-1}	4.36×10^{-1}

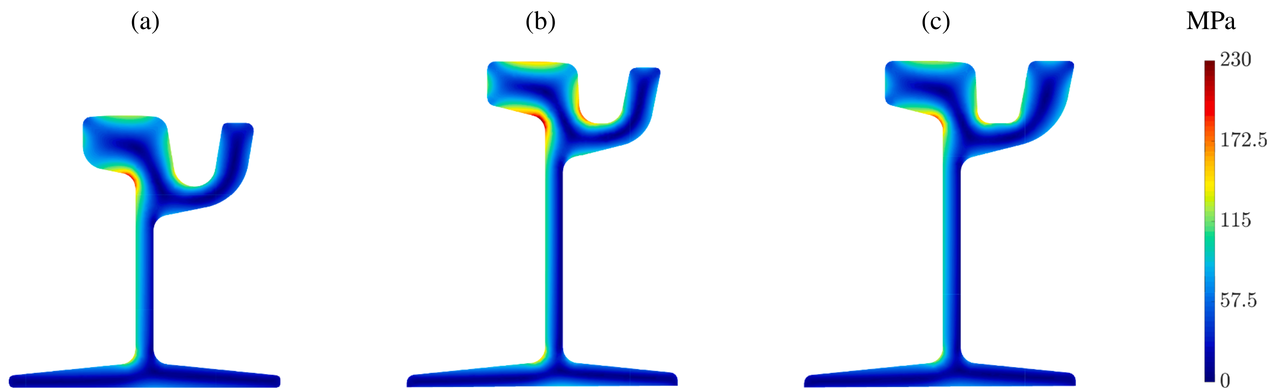

Fig. 8. Distributions of von Mises stresses σ_{vM} in a rail along a right-curved rail track in response to a typical load case for profiles (a) 60R1, (b) 60R3, (c) 63R1.

Fig. 9. Photograph of an excavated tramway rail showing a long crack running approximately parallel to rail axis in an 18-year-old, right-curved rail of profile 60R1, by courtesy of Wiener Linien GmbH & Co KG.

generalized beam model could also consider the effects of an elastic foundation, as well as temperature effects, and the influence of (longitudinal) residual stresses. Particularly, the latter task is highly challenging. Hence, approaching this issue based on residual stresses found in experimental studies [25,69–71] seems to be a reasonable strategy for eventually assessing the contribution of residual stresses to rail fractures.

- The critical loading scenario presented in Section 6 is thought to underline the practicability of our method. Once the aforementioned extension to a full 3D analysis is completed, more realistic scenarios can be simulated, such as emergency braking, potentially involving significant longitudinal forces.
- While the current paper focusses on the computation of stress peaks in rails which may lead to macroscopic rail fractures that are observed *in situ*, future research activities may also include studying the post-cracking behavior, based on the wealth of respective works reported in literature, on both brittle materials, see, e.g., [72–75], and ductile materials, see, e.g., [76–78].

Acknowledgments

Financial support by Wiener Linien GmbH & Co KG is gratefully acknowledged.

Appendix A. Nomenclature

Abbreviations

FE	Finite Element
GC	geometrical center
SC	shear center

Latin symbols

a_y, a_z	proportionality factors related to shear forces
A	cross-sectional area
A_{ij}	second-order area moments, with $i, j = x, y, z$
E	Young's modulus
$\mathbf{e}_x$, $\mathbf{e}_y$, $\mathbf{e}_z$	unit vectors associated to the longitudinal, horizontal and vertical beam axes
e_y, e_z	eccentricities of shear forces S_z and S_y with respect to SC
$\mathbf{F}^{S,i}$	force vector of the shear problem
$\mathbf{F}^{M_T,i}$	force vector of the torsional problem
G	shear modulus
g	gravitational acceleration
$\mathscr{H}^1$	Sobolev space
I_T	torsional inertia moment
K	bulk modulus
$\mathbf{K}^{S,i}$	stiffness matrix of the shear problem
$\mathbf{K}^{M_T,i}$	stiffness matrix of the torsional problem
M_T	torsional moment with respect to SC
$\mathbf{N}$	row vector of shape functions for the isoparametric four-noded bilinear quadrilateral finite element

$\mathbf{n}$	unit normal vector
n_y, n_z	components of the unit normal vector in the cross-sectional plane
n_{el}	total number of elements
R	curvature radius
s^{el}	outer boundary of contour finite element
S_y	horizontal shear force
$S_{y,0}$	horizontal unit shear force of 1 kN
S_z	vertical shear force
$S_{z,0}$	vertical unit shear force of 1 kN
v	velocity of tramway car wheel
$\mathbf{x}$	location vector
x	Cartesian coordinate along beam axis with origin in GC
y, z	Cartesian coordinates perpendicular to beam axis with origin in GC
$\bar{y}$, $\bar{z}$	Cartesian coordinates perpendicular to beam axis with origin in left bottom corner of cross section
y^i, z^i	coordinates approximated across finite element
$\mathbf{y}^i$, $\mathbf{z}^i$	vectors comprising nodal coordinate values in finite element
y_{SC}, z_{SC}	coordinates of SC in Cartesian coordinate system with origin in GC
$\bar{y}_{GC}$, $\bar{z}_{GC}$	coordinates of GC in Cartesian coordinate system with origin in left bottom corner of cross section

Greek symbols

ε_{xx}, ε_{yy}, ε_{zz}	normal components of strain tensor
ε_{xy}, ε_{xz}, ε_{yz}	shear components of strain tensor
ε_{xy}^S, ε_{xz}^S	shear force-induced shear strain components in cross-sectional plane
γ_{xy}, γ_{xz}	shear strains in cross-sectional plane
γ_{xy}^S, γ_{xz}^S	shear force-induced shear strains in cross-sectional plane
ϑ	twist of the beam
ν	Poisson's ratio
σ_{vM}	von Mises stress
σ_{xx}	normal stress component in longitudinal beam direction
σ_{xy}, σ_{xz}	shear stress components in cross-sectional plane
$\sigma_{xy}^{M_T}$, $\sigma_{xz}^{M_T}$	torsion-induced shear stress components in cross-sectional plane
σ_{xy}^S, σ_{xz}^S	shear force-induced shear stress components in cross-sectional plane
Υ	test function space of 2D FE method
Φ	test function
Φ^i	test function approximated across finite element
$\boldsymbol{\Phi}^i$	vector comprising nodal Φ-values in finite element
ω^S	shear warping function
$\omega^{S,i}$	shear warping function approximated across finite element
$\boldsymbol{\omega}^{S,i}$	vector comprising nodal ω^S-values in finite element
ω^{M_T}	torsional warping function
$\omega^{M_T,i}$	torsional warping function approximated across finite element
$\boldsymbol{\omega}^{M_T,i}$	vector comprising nodal $\omega^{M_T,i}$-values in finite element
Ω	cross-sectional domain
Ω^{el}	domain of finite element
$\partial\Omega$	cross-sectional contour

Operators

A	assembly operator
Δ	Laplace operator

References

[1] Topp HH. Innovations in tram and light rail systems. Proc Inst Mech Eng Part F: J Rail Rapid Transit 1999;213(3):133–41.
[2] Hattori S. Trams making way for light rail transit. Japan Railway Transport Rev 2004;38:30–40.
[3] Lichtenegger M. Tram, bus, metro: Wiener Linien offers one of Europe's densest networks. Public Transport Int 2009;58:12–3.
[4] Steinbauer G, Ossberger M, Dorazin D. Prozessmanagement individuell umgesetzt [Process Management Employed Individually], chapter Wiener Linien: Infrastruktur für den öffentlichen Verkehr bereitstellen: Prozessmanagement mit hoher Komplexität [Wiener Linien: providing infrastructure for public transit: high-complexity process management]. Springer Berlin Heidelberg; 2005. p. 221–36 [In German].
[5] Beretta S, Braghin F, Bucca G, Desimone H. Structural integrity analysis of a tramway: load spectra and material damage. Wear 2005;258(7):1255–64.
[6] Popović Z, Popović V. Analysis of cracking on running surface of rails. Gradevinar 2013;65(3):251–9.
[7] Yousefikia M, Moridpour S, Setunge S, Mazloumi E. Modeling degradation of tracks for maintenance planning on a tram line. J Traffic Log Eng 2014;2(2):86–91.
[8] Chiacchiari L, Loprencipe G. Measurement methods and analysis tools for rail irregularities: a case study for urban tram track. J Modern Transport 2015;23(2):137–47.
[9] Kalker JJ. Wheel-rail rolling contact theory. Wear 1991;144(1):243–61.
[10] Bernasconi A, Davoli P, Filippini M, Foletti S. An integrated approach to rolling contact sub-surface fatigue assessment of railway wheels. Wear 2005;258(7–8):973–80.
[11] Jin X, Wen Z, Xiao X, Zhou Z. A numerical method for prediction of curved rail wear. Multibody Syst Dyn 2007;18(4):531–57.
[12] Hinteregger E. Eigenspannungen und Verformungen in Schienen nach dem Walzen vor dem Richten [Residual stresses and distortion of rails after rolling before straightening]. Phd thesis. Montanuniversität Leoben, Austria; 1990 [In German].
[13] Bower AF, Johnson KL. Shakedown, residual stress and plastic flow in repeated wheel-rail contact. In: Kalker JJ, Cannon DF, Orringer O, editors. Rail quality and maintenance for modern railway operation. Dordrecht: Springer Science and Business Media; 1993. p. 239–49.
[14] Finstermann G, Fischer FD, Shan G, Schleinzer G. Residual stresses in rails due to roll straightening. Steel Res 1998;69(7):272–8.
[15] Schleinzer G, Fischer FD. Residual stresses in new rails. Mater Sci Eng: A 2000;288(2):280–3.
[16] Schleinzer G, Fischer FD. Residual stress formation during the roller straightening of railway rails. Int J Mech Sci 2001;43(10):2281–95.
[17] Fischer FD, Schleinzer G. Residual stress formation and distortion of rail steel. In: Totten G, Howes M, Inoue T, editors. Handbook of Residual Stress and Deformation of Steel. ASM International; 2002. p. 424–36.
[18] Betegón Biempica C, del Coz Díaz JJ, García Nieto PJ, Peñuelas Sánchez I. Nonlinear analysis of residual stresses in a rail manufacturing process by FEM. Appl Math Model 2009;33(1):34–53.
[19] Pernía-Espinoza AV. Use of advanced numerical simulation techniques for the study and improvement of steel-profiles manufacturing processes. Phd thesis. Universidad de la Rioja, Spain; 2007.
[20] Webster PJ, Wang X, Mills G, Webster GA. Residual stress changes in railway rails. Phys B: Condens Matter 1992;180:1029–31.
[21] Esveld C. Modern Railway Track. 2nd ed. MRT-Productions; 2001 chapter 10.2.6. p. 282–5.
[22] Orringer O, Paxton WR, Gray DE, Raj PK. Residual stress and its consequences on both sides of the wheel-rail interface. Wear 1996;191(1):25–34.
[23] Ringsberg JW, Bjarnehed H, Johansson A, Josefson BL. Rolling contact fatigue of rails – finite element modelling of residual stresses, strains and crack initiation. Proc Inst Mech Eng, Part F: J Rail Rapid Transit 2000;214(1):7–19.
[24] Ranjha SA, Mutton P, Kapoor A. Effect of head wear and lateral forces on underhead radius crack propagation. Proc Inst Mech Eng, Part F: J Rail Rapid Transit 2014;228(6):620–30.
[25] Magiera J, Orkisz J, Karmowski W. Reconstruction of residual stresses in railroad rails from measurements made on vertical and oblique slices. Wear 1996;191(1):78–89.
[26] Yu C-C, Keer LM, Steele RK. Three-dimensional residual stress effects on the fatigue crack initiation in rails. J Tribol 1997;119(4):660–6.
[27] Skyttebol A, Josefson BL, Ringsberg JW. Fatigue crack growth in a welded rail under the influence of residual stresses. Eng Fract Mech 2005;72(2):271–85.
[28] Sih GC, Da-Yu Tzou D-Y. Three-dimensional transverse fatigue crack growth in rail head. Theor Appl Fract Mech 1984;1(1):103–15.
[29] Fischer FD, Sun Q-P, Tanaka K. Transformation-induced plasticity (TRIP). Appl Mech Rev 1996;49(6):317–64.
[30] Fischer FD, Reisner G, Werner E, Tanaka K, Cailletaud G, Antretter T. A new view on transformation induced plasticity (TRIP). Int J Plast 2000;16(7):723–48.
[31] Eisenmann J. Teil II: Die Schiene als Träger und Fahrbahn – Theoretische Grundlagen und praktische Beispiele [Part II: The railway as carrier and roadway – theoretical basics and practical examples]. In: Fastenrath F, editor. Die Eisenbahnschiene [The Railroad Track]. Verlag von Wilhelm Ernst & Sohn Berlin, München, Düsseldorf, Germany; 1977. p. 1–78 [In German].
[32] Transportation Research Board. Track Design Handbook for Light Rail Transit. Technical report. Washington, D.C.; 2000.
[33] Matthews V. Bahnbau [Railway Construction], Teubner Studienskripten Bauwesen. Vieweg + Teubner Verlag, Wiesbaden, Germany; 2007 [In German].

[34] ÖNORM EN 14811. Ausgabe: 2010-05-01: Bahnanwendungen – Oberbau – Spezialschienen – Rillenschienen und zugehörige Konstruktionsprofile [Railway Applications – Track Structures – Special Rails – Grooved Rails and Construction Profiles]. Austrian Standards Institute, Vienna, Austria; 2010 [In German].
[35] Cheli F, Corradi R, Diana G, Facchinetti A. Validation of a numerical model for the simulation of tramcar vehicle dynamics by means of comparison with experimental data. J Comput Nonlinear Dyn 2007;2(4):299–307.
[36] Ignesti M, Marini L, Meli E, Rindi A. Development of a model for the prediction of wheel and rail wear in the railway field. J Comput Nonlinear Dyn 2012;7(4):1–14.
[37] Kouroussis G, Pauwels N, Brux P, Conti C, Verlinden O. A numerical analysis of the influence of tram characteristics and rail profile on railway traffic ground-borne noise and vibration in the Brussels region. Sci Total Environ 2014;482–483:452–60.
[38] Lojkowski W, Djahanbakhsh M, Bürkle G, Gierlotka S, Zielinski W, Fecht H-J. Nanostructure formation on the surface of railway tracks. Mater Sci Eng: A 2001;303(1–2):197–208.
[39] Elwazri AM, Wanjara P, Yue S. The effect of microstructural characteristics of pearlite on the mechanical properties of hypereutectoid steel. Mater Sci Eng: A 2005;404(1):91–8.
[40] Çalik A. Effect of cooling rate on hardness and microstructure of AISI 1020, AISI 1040 and AISI 1060 steels. Int J Phys Sci 2009;4:514–8.
[41] Schröder R. Influences on development of thermal and residual stresses in quenched steel cylinders of different dimensions. Mater Sci Technol 1985;1(10):754–64.
[42] Bhadeshia HKDH, Honeycombe RWK. Material factors. In: Totten G, Howes M, Inoue T, editors. Handbook of Residual Stress and Deformation of Steel. 3rd ed.Oxford, UK: Butterworth-Heinemann; 2002. p. 3–10.
[43] Kim SA, Johnson WL. Elastic constants and internal friction of martensitic steel, ferritic-pearlitic steel, and α-iron. Mater Sci Eng: A 2007;452–453:633–9.
[44] Pham T-H, Kim S-E. Determination of mechanical properties in SM490 steel weld zone using nanoindentation and FE analysis. J Constr Steel Res 2015;114:314–24.
[45] Pham T-H, Kim JJ, Kim S-E. Estimating constitutive equation of structural steel using indentation. Int J Mech Sci 2015;90:151–61.
[46] Brenner SS. Tensile strength of whiskers 1957; 27: 1484–91.
[47] Bhadeshia HKDH, Honeycombe RWK. Strengthening of iron and its alloys. In: Bhadeshia HKDH, Honeycombe RWK, editors. Steels: Microstructure and Properties. 3rd ed.Butterworth-Heinemann; 2006. p. 17–38.
[48] Timoshenko SP. History of strength of materials: with brief account of the history of elasticity and theory of structures. Dover Publications; 1953.
[49] Gruttmann F, Sauer R, Wagner W. Shear stresses in prismatic beams with arbitrary cross-sections. Int J Numer Meth Eng 1999;45(7):865–89.
[50] Gruttmann F, Wagner W. Shear correction factors in Timoshenko's beam theory for arbitrary shaped cross-sections. Comput Mech 2001;27(3):199–207.
[51] Kourtis LC, Kesari H, Carter DR, Beaupré GS. Transverse and torsional shear stresses in prismatic bodies having inhomogeneous material properties using a new 2D stress function. J Mech Mater Struct 2009;4(4):659–74.
[52] Reddy JN, Chin CD. Thermomechanical analysis of functionally graded cylinders and plates. J Therm Stress 1998;21(6):593–626.
[53] Kourtis L, Carter D, Kesari H, Beaupre GS. A new software tool (VA-BATTS) to calculate bending, axial, torsional and transverse shear stresses within bone cross sections having inhomogeneous material properties. Comput Meth Biomech Biomed Eng 2008;11:463–76.
[54] Sladek V, Sladek J, Atluri SN, Van Keer R. Numerical integration of singularities in meshless implementation of local boundary integral equations. Comput Mech 2000;25(4):394–403.
[55] Sapountzakis EJ. Bars under torsional loading: a generalized beam theory approach. ISRN Civil Eng 2013;2013(916581):1–39.
[56] Liszka T, Orkisz J. The finite difference method at arbitrary irregular grids and its application in applied mechanics. Comput Struct 1980;11(1):83–95.
[57] Sladek J, Sladek V, Atluri SN. A pure contour formulation for the meshless local boundary integral equation method in thermoelasticity. CMES – Comput Meth Eng Sci 2001;4:423–33.
[58] Sladek J, Sladek V, Zhang C. Transient heat conduction analysis in functionally graded materials by the meshless local boundary integral equation method. Comput Mater Sci 2003;28(3–4):494–504.
[59] Milewski S. Meshless finite difference method with higher order approximation – applications in mechanics. Arch Comput Meth Eng 2012;19(1):1–49.
[60] Belytschko T, Krongauz Y, Organ D, Fleming M, Krysl P. Meshless methods: an overview and recent developments. Comput Meth Appl Mech Eng 1996;139(1):3–47.
[61] Nguyen VP, Rabczuk T, Bordas S, Duflot M. Meshless methods: a review and computer implementation aspects. Math Comput Simul 2008;79(3):763–813.
[62] Brézis H. Functional Analysis, Sobolev Spaces and Partial Differential Equations. New York: Springer; 2011.
[63] Bathe KJ. Finite Element Procedures. Watertown, MA, 2nd ed.; 2014.
[64] Wiener Linien GmbH & Co KG. Achslast Typenübersicht [Axle Load Type Overview]. Internal documentation; 2012 [In German].
[65] Landau LD, Lifshitz EM. Mechanics. 3rd ed. Oxford: Butterworth-Heinemann; 1976.
[66] Hand LN, Finch JD. Analytical Mechanics. Cambridge University Press; 1998.
[67] Wiener Linien GmbH & Co KG. STRAB Richtlinien betreffend höchstzulässige Fahrgeschwindigkeiten im Straßenbahnbetrieb [STRAB Guidelines concerning maximum vehicle speed in tramway operation]. Internal documentation; 2000 [In German].
[68] Wiener Linien GmbH & Co KG. Mitarbeiterschulung – Wagenkunde [Employee Training – Vehicle Information]. Internal documentation; 1994 [In German].
[69] Magiera J. Enhanced 3D analysis of residual stress in rails by physically based fit to neutron diffraction data. Wear 2002;253(1):228–40.
[70] Skrzat A, Orkisz J. Reconstruction of residual hoop stress in railroad car wheels based on saw cut measurements. Exp Mech 2009;49(4):491–9.
[71] Pazdanowski M. On estimation of residual stresses in rails using shake-down based method. Arch Transport 2010;22:319–36.
[72] Dumstorff P, Meschke G. Crack propagation criteria in the framework of X-FEM-based structural analyses. Int J Numer Anal Meth Geomech 2007;31(2):239–59.
[73] Meschke G, Dumstorff P. Energy-based modeling of cohesive and cohesionless cracks via X-FEM. Comput Meth Appl Mech Eng 2007;196(21–24):2338–57.
[74] Theiner Y, Hofstetter G. Numerical prediction of crack propagation and crack widths in concrete structures. Eng Struct 2009;31(8):1832–40.
[75] Theiner Y, Hofstetter G. Modellierung der Rissbildung in Betonstrukturen [Modelling of cracking in concrete structures]. Bauingenieur 2010;85:150–8. [In German].
[76] Rousselier G. Ductile fracture models and their potential in local approach of fracture. Nucl Eng Des 1987;105(1):97–111.
[77] Chaboche JL. Continuum damage mechanics: Part II – Damage growth, crack initiation, and crack growth. J Appl Mech 1988;55(1):65–72.
[78] Ritchie RO. Mechanisms of fatigue-crack propagation in ductile and brittle solids. Int J Fract 1999;100(1):55–83.